ICARUS 101, 244–264 (1993)

Motion of Dust in a Planetary Magnetosphere: Orbit-Averaged Equations for Oblateness, Electromagnetic, and Radiation Forces with Application to Saturn's E Ring

DOUGLAS P. HAMILTON

Cornell University, Ithaca, New York 14853

Received August 14, 1992; revised November 11, 1992

In this paper, we apply orbital perturbation theory to the circumplanetary motion of micrometer-sized dust grains subject to gravitational, electromagnetic, and radiation forces. We extend the orbit-averaged radiation pressure equations of Mignard (1982, *Icarus* 49, 347–366) to include planetary obliquity. We also derive new equations for the Lorentz force arising from the aligned dipolar and quadrupolar components of the planetary magnetic field. Following these derivations, we provide a framework for combining all perturbations and demonstrate the validity of the resulting expressions by comparing numerical integrations of them to integrations of the full Newtonian equations; typically the orbit-averaged equations can be integrated several hundred times faster. Finally, we analytically and numerically apply the newly derived equations to particles moving through the Saturnian E ring and discuss implications for that ring's azimuthal and vertical structure. It is argued that the behavior of orbital precession rates at large eccentricities leads to azimuthal asymmetry in the E ring. Furthermore, a peculiar locking of orbital pericenters out of the equatorial plane is shown to have implications for the E ring's vertical structure. We show analytically that the locking is caused by small vertical forces arising from radiation pressure and from the planet's aligned quadrupolar field. Because the normal component of radiation pressure varies over Saturn's orbital period, we suggest that the vertical structure of the E ring varies with time.

1. GENERAL REMARKS ON DUST AND ORBITAL PERTURBATION THEORY

Although dust particles contain only a tiny fraction of the mass in orbit about a planet, they far outnumber their macroscopic companions. In planetary systems these tiny motes are ubiquitous, both interspersed with macroscopic bodies in optically thick rings and organized into tenuous structures of their own. Sensitive detectors aboard spacecraft have discovered dust strewn throughout planetary systems in quantities too faint to be visible (Gurnett *et al.* 1983, 1986, 1989). Clearly the overall distribution of dust in circumplanetary orbits is complex; yet the distribution, and the fact that it can indicate the presence of larger, perhaps unseen, source bodies are of interest to diverse groups of researchers. Ring dynamicists hope to understand the dominant processes operating in faint dust bands, some of which may be relevant to the optically thick classical ring systems. Magnetospheric physicists are interested in the distribution of plasma close to the planet; in this locale dust grains can be important sources and sinks for charged particles. Finally, the impact of numerous grains can damage a spacecraft by scouring its optical components; slightly larger objects can damage other instruments. These considerations must be weighed carefully by mission planners and engineers wishing to assess risks. Knowledge of the distribution of dust in circumplanetary orbits is useful to all of these researchers; a necessary prerequisite for such knowledge is a good understanding of the orbital dynamics of an individual dust grain. The first several sections of this paper provide a framework for studying orbital perturbations on dust grains located throughout the circumplanetary environment. In the final sections, we apply these general results to the specific case of dust in the Saturnian E ring.

Micrometer-sized dust grains moving along circumplanetary orbits are subject to strong nongravitational perturbations due to scattering of solar photons and due to Lorentz forces arising from the planet's rotating magnetic field. The effect of these perturbations on an orbiting dust particle can be determined by including the perturbation forces in the left-hand side of Newton's second law $\mathbf{F} = m\mathbf{a}$. In general this equation cannot be solved analytically, so we are forced to resort to approximate or numerical methods (see Hamilton and Burns 1992, Horanyi *et al.* 1992, Schaffer and Burns 1992, among others). In many cases, however, we are interested not in detailed information on how a particle's position and velocity change with time but only in how the character of its orbit varies. In these cases, the six *osculating* orbital elements (a, e, i, Ω,

0019-1035/93 $5.00

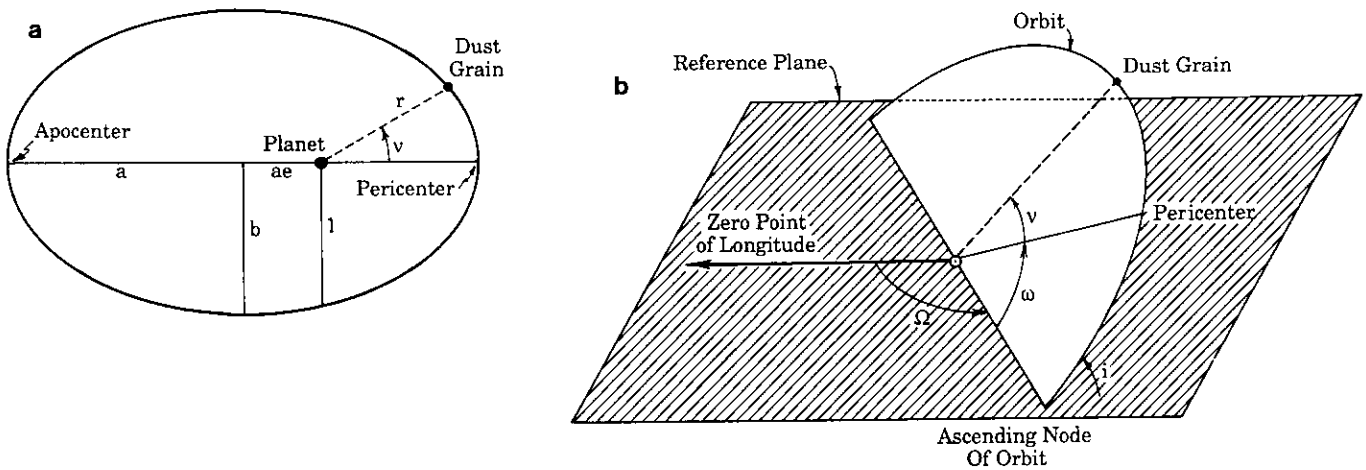

FIG. 1. (a) View of an elliptical orbit in the orbital plane. Three of the orbital elements—the semimajor axis a, eccentricity e, and true anomaly ν—are depicted. Simple geometry shows that the orbit center is offset from the planet by a distance ae, the semiminor axis is given by $b = a(1 - e^2)^{1/2}$, and the semi-latus rectum by $l = a(1 - e^2)$. (b) Three additional orbital elements that define the orientation of an elliptical orbit relative to a fixed plane and a reference direction in that plane. The longitude of the ascending node, Ω, measures the angle from the reference direction to the point where the orbit's plane intersects the reference plane; the argument of pericenter, ω, defines the angle between that intersection point and pericenter (the closest approach of the orbit to the central body); and the inclination, i, measures the angle between the orbital and reference planes. Inclination is defined such that $0° \leq i \leq 180°$.

ω, and ν) defined in Figs. 1a and 1b are particularly useful. Other choices for these elements, especially the sixth, are also possible (Danby 1988, p. 201). We often use $\mathcal{M} \equiv nt$, the *mean anomaly*, where $n = (\mu/a^3)^{1/2}$ is the particle's mean motion, t is the time measured from the moment of pericenter passage, and μ is the product of the gravitational constant G and the planetary mass M_p.

If the perturbation forces are small compared to the planet's gravitational attraction, the first five osculating elements change slowly over timescales much longer than the particle's orbital period. Therein lies the primary advantage of the orbital elements: because they are connected to the geometry of the orbit and because they vary slowly with time, the osculating elements allow a direct visualization of the orbital history of a perturbed body in a way that far surpasses that possible with a set of positions and velocities. Take, for example, the case of an orbit around an oblate planet which we discuss in Section 2. It is well known that the orbit-averaged solution to this problem is, to high accuracy, simply a precessing ellipse (Danby 1988, p. 345). The orbit retains its size, shape, and inclination off the equatorial plane while its node regresses and its pericenter precesses, each at a constant rate. By calculating these rates from equations given below and using Figs. 1a and 1b, one can easily picture the resulting orbital evolution. Attaining the same picture from positions and velocities as functions of time requires more computation and considerably greater insight!

We note that, technically, the osculating elements differ slightly from *geometric elements* which describe the true shape of the orbit; these derivations are of order of the dimensionless ratio (ε) of the perturbing force to gravity. For an oblate planet, therefore, the discrepancies are of order J_2 (see Greenberg 1981, Borderies and Longaretti 1987). These differences are especially important when true eccentricities and inclinations are small compared to ε (*e.g.*, a particle on the geometrically circular orbit discussed by Greenberg (1981) has a small osculating eccentricity and appears as if it is always at its osculating pericenter), and when other perturbations do not strongly affect an element. Similarly, the rate of change of the mean anomaly is unequal to the mean motion for perturbed orbits; the deviations are of order ε and are due both to real changes in a particle's speed and to differences between the osculating and geometric elements. Because we are primarily interested in how a particle's orbit evolves, we will not use the mean anomaly perturbations in this paper, but merely include them in the equations to follow for completeness.

The fact that, for modest perturbations, the osculating orbital elements vary slowly in time is useful both numerically and analytically because it allows the effects of a perturbation to be averaged over a single (assumed constant) Keplerian orbit. The resulting averaged expressions describe how the osculating orbital elements change in time and are accurate to first order in ε. In the following sections we treat the strongest perturbation forces acting on close circumplanetary dust grains—higher-order gravity, radiation pressure, and the electromagnetic force—and derive the appropriate orbit-averaged equations.

2. HIGHER ORDER GRAVITY

Treatments of the orbital perturbations arising from nonspherical terms in a planet's gravitational field can be found in many texts (*e.g.*, Danby 1988), but we include a short discussion of them in this section both for completeness and to provide a simple example of the orbit-averaging process that can be compared with the more complicated ones to follow.

Because a planet's spin is responsible for most of the distortion of its gravity field, the field can be well represented by adding an axially symmetric perturbing potential,

$$V_{GR} = -\frac{\mu}{r}\sum_{j=2}^{\infty} J_j \left(\frac{R_p}{r}\right)^j P_j(\cos\theta), \tag{1}$$

to the standard point source potential; the perturbing force is obtained by taking the gradient: $\mathbf{F}_{GR} = -m_g \nabla V_{GR}$. Throughout this paper the subscripts "p" and "g" stand for "planet" and "grain," respectively; here R_p is the planet's radius and m_g is the mass of the dust grain. The $P_j(x)$ are Legendre polynomials and the J_j are dimensionless coefficients that can be evaluated for a particular planet to describe its gravity field.

To derive the first-order orbit-averaged equations, we rewrite the potential, Eq. (1), in terms of the orbital elements and average it over time to obtain the negative of the disturbing function. Inserting the disturbing function into the potential form of the planetary equations (Danby 1988, p. 336), we find the equations for the variation of the elements

$$\left\langle \frac{da}{dt} \right\rangle_{J_2} = 0, \tag{2a}$$

$$\left\langle \frac{de}{dt} \right\rangle_{J_2} = 0, \tag{2b}$$

$$\left\langle \frac{di}{dt} \right\rangle_{J_2} = 0, \tag{2c}$$

$$\left\langle \frac{d\Omega}{dt} \right\rangle_{J_2} = -\frac{3nJ_2R_p^2}{2a^2(1-e^2)^2}\cos i, \tag{2d}$$

$$\left\langle \frac{d\omega}{dt} \right\rangle_{J_2} = \frac{3nJ_2R_p^2}{2a^2(1-e^2)^2}\left(2 - \frac{5}{2}\sin^2 i\right), \tag{2e}$$

$$\left\langle \frac{dM}{dt} - n \right\rangle_{J_2} = \frac{3nJ_2R_p^2}{2a^2(1-e^2)^{3/2}}\left(1 - \frac{3}{2}\sin^2 i\right), \tag{2f}$$

where the angular brackets denote orbit-averaged quantities (*cf.* Danby 1988, p. 347). Technically, each of the orbital elements at the right side of Eqs. (2a–f) should be encased in angled brackets as we ignore their short period fluctuations, but these brackets will be omitted for clarity since we refer only to the averaged elements throughout this paper.

Notice that Eqs. (2a–f) are trivially integrable even though the full problem is not (Kozai 1959). The first three expressions imply that the elements a, e, and i are constant and, consequently, the right-hand sides of the final three equations are also fixed. Thus the angles Ω and ω circulate, having values that change linearly in time. Since the circulation times are $\sim(a/R_p)^2/J_2$ times longer than the orbital period, the solution to Eqs. (2a–e) is simply a slowly rotating ellipse.

The final equation merely expresses the average rate at which a particle completes a single osculating orbit from pericenter to pericenter; the rate differs slightly from the mean motion both because the particle's average angular speed is changed and because the position of pericenter slowly shifts. For equatorial orbits, the right-hand side of Eq. (2f) is positive and the particle completes its radial pericenter-to-pericenter oscillation slightly faster than its unperturbed Keplerian counterpart. This is an expected result since planetary oblateness augments the inward pull of point-source gravity; the increased force effectively raises the oscillator's "spring constant" and hence its frequency.

3. RADIATION PRESSURE

For micron-sized grains in circumplanetary orbit, solar radiation pressure is a strong perturber. In its simplest form, radiation pressure imparts a force on a grain given by

$$\mathbf{F}_{RP} = -\beta \frac{GM_\odot}{R^2}\hat{\mathbf{s}}, \tag{3}$$

where $M_\odot$ is the solar mass, R is the Sun–planet distance, $\hat{\mathbf{s}}$ is a unit vector pointing from the planet toward the Sun, and β is the dimensionless ratio of the radiation force to solar gravity. For our Sun, Burns *et al.* (1979) express

$$\beta = 5.7 \times 10^{-5}\frac{Q_{pr}}{\rho_g r_g}, \tag{4}$$

which is valid for spherical particles that obey geometrical optics ($r_g \gtrsim 0.5\mu m$). Here r_g and ρ_g are the particle's radius and density, and Q_{pr} is a constant near unity whose exact value depends on the optical properties of the grain. The simple expressions given above ignore the anisotropy of reradiated photons (Poynting–Robertson drag), grain ro-

tation (Yarkovsky effect), the planetary shadow, and complications arising from the rotation and finite angular size of the Sun. These effects are quite small compared to the main force of radiation pressure and can usually be neglected in a first approximation. Despite the fact that they are weak, dissipative forces, such as Poynting–Robertson drag can be important because they affect the semimajor axis, an element unperturbed by direct radiation pressure. Similarly, effects of the planet's shadow make it possible for radiation pressure to alter the semimajor axis of an orbit (Mignard 1984, Horanyi and Burns 1991). Nevertheless, for the times of a few tens of years considered here, it is legitimate to ignore these weak forces.

Orbit-averaged solutions to a particle moving around a spherical planet subject to that planet's gravity and solar radiation pressure have been derived by several authors including Burns *et al.* (1979) and Chamberlain (1979), both of whom used Gauss' form of Lagrange's planetary equations for a force constant in magnitude and direction, and Mignard (1982), who used a disturbing function approach and included the effects of solar motion. All of the above authors did their analysis in the plane defined by the orbital motion of the planet around the Sun (hereafter called the ecliptic plane[1]) and measured their inclinations from that plane. In the case of motion about an oblate planet, however, the planet's equatorial plane is also important—this is especially true since most sources of circumplanetary dust (planetary rings and inner satellites) reside near this plane. It is natural, therefore, to seek an orbit-averaged solution to the orbital evolution caused by radiation pressure that can be expressed in the planet's equatorial plane; this is equivalent to adding a nonzero planetary obliquity, γ, to the previously derived solutions. In this section we discuss two approaches to obtaining equatorial equations and then we derive analytical expressions valid for all obliquities.

One approach, motivated by the fact that orbit-averaged equations valid in the ecliptic plane are already available (Mignard 1982), is to simply translate these equations into the equatorial plane; this task can only be accomplished if the orbital elements themselves can be converted. Since the new set of elements describe the same elliptical orbit from a different reference plane, only the angles (i, Ω, and ω) that define the orbit's orientation relative to the plane will be altered (Fig. 1b)—the other elements (a, e, and ν) will be identical in both frames. We seek, therefore, functions that relate the new orientation angles to the old. These can be obtained either by simple rotations or from spherical trigonometry. As seen from

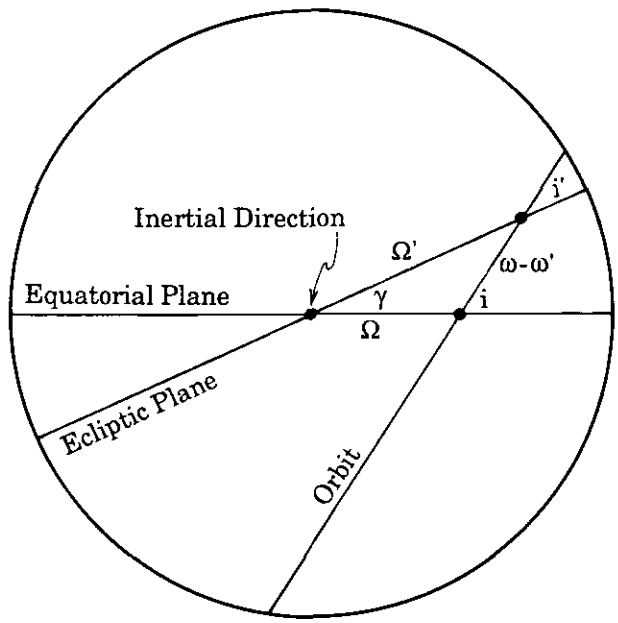

FIG. 2. The planet's equatorial plane, the ecliptic plane, and the dust grain's orbital plane, each as projected onto the sky from the planet's center. Elements describing the orientation of the grain's orbital plane relative to either of the two reference planes are shown; in each case, the inertial reference direction is the ascending node of the ecliptic on the equatorial plane. Primed quantities are elements referenced to the ecliptic plane, unprimed ones are measured along (or from) the equatorial plane, and γ is the planet's obliquity. The spherical triangle formed by the intersections of these three planes implicitly define one set of elements in terms of the other $[(i,\Omega,\omega) \rightarrow (i',\Omega',\omega')]$.

the planet's center, the equatorial plane, the ecliptic plane, and a particle's orbital path all appear as great circles on the sky (Fig. 2); for simplicity we have chosen to measure each orbital node from the ascending node of the ecliptic on the equatorial plane. The spherical triangle formed by the intersections of these great circles implicitly defines the equatorial elements in terms of the ecliptic elements. Unfortunately, the expressions resulting from translating to equatorial elements are cumbersome enough to defeat the main purpose of orbit-averaging, which is to obtain simple equations for analytic work. Accordingly, we try a different tack.

Since we hope to combine the effects of radiation pressure with those of other perturbations, we need orbit-averaged expressions referenced to the equatorial plane and to an inertial direction. We choose a right-hand coordinate system centered on the planet with $\hat{\mathbf{x}}$ pointing to the ascending node of the ecliptic on the equatorial plane (Fig. 2), $\hat{\mathbf{y}}$ in the equatorial plane, and $\hat{\mathbf{z}}$ along the spin axis. Since, to a good approximation, the Sun is motionless during the time it takes the particle to complete a single orbit (this will only be inaccurate for very distant orbits), we can average over an orbital period while hold-

[1] Here we use the term ecliptic somewhat loosely to avoid confusion between the planet and particle orbital planes. Strictly speaking, the ecliptic refers only to Earth's orbital plane.

ing the Sun's position constant. The problem breaks down into three pieces: (1) determine the response of the orbit to a constant force along each of the coordinate axes; (2) solve for the Sun's motion in the equatorial frame; and (3) linearly combine these solutions.

Starting the first task, we resolve the solar position in the equatorial frame into components with magnitudes s_x, s_y, and s_z, the time variable values of which will be determined shortly. The solar position as seen from this frame is then simply $\hat{\mathbf{s}} = s_x\hat{\mathbf{x}} + s_y\hat{\mathbf{y}} + s_z\hat{\mathbf{z}}$. The perturbing potential V_{RP} is obtained from Eq. (3) via the relation $\mathbf{F}_{RP} = -\nabla V_{RP}$. Since the magnitude and direction of radiation pressure change only slightly over a single orbit of the dust grain, we treat the right-hand side of Eq. (3) as a constant and find $V_{RP} = F_{RP}(s_x x + s_y y + s_z z)$. To average the disturbing function, $-V_{RP}$, over time, we first need to express the cartesian coordinates x, y, z in terms of orbital elements:

$$x = r\sin\theta\cos\phi = r(\cos\Omega\cos u - \sin\Omega\sin u\cos i), \quad (5)$$

$$y = r\sin\theta\sin\phi = r(\sin\Omega\cos u + \cos\Omega\sin u\cos i), \quad (6)$$

$$z = r\cos\theta = r\sin i\sin u, \quad (7)$$

where

$$r = \frac{a(1-e^2)}{1 + e\cos\nu}, \quad (8)$$

and $u \equiv \omega + \nu$ is the *argument of latitude*. Since s_x, s_y, and s_z are nearly constant during the time it takes a dust grain to make a single circuit around the planet, only the following orbital time-averages are needed:

$$\langle x\rangle = -\tfrac{3}{2}ea(\cos\Omega\cos\omega - \sin\Omega\sin\omega\cos i), \quad (9a)$$

$$\langle y\rangle = -\tfrac{3}{2}ea(\sin\Omega\cos\omega + \cos\Omega\sin\omega\cos i), \quad (9b)$$

and

$$\langle z\rangle = -\tfrac{3}{2}ea\sin i\sin\omega. \quad (9c)$$

We note that $\langle y\rangle$ can be obtained from $\langle x\rangle$ by subtracting 90° from the node in Eq. (9a) and that all expressions reduce appropriately if e or i equals zero. Inserting these expressions into the potential formulation of the planetary equations, we obtain (after some algebra) the following expressions for the variation of the orbital elements:

$$\left\langle\frac{da}{dt}\right\rangle_{RP} = 0, \quad (10a)$$

$$\left\langle\frac{de}{dt}\right\rangle_{RP} = \alpha(1-e^2)^{1/2}[s_x(\cos\Omega\sin\omega + \sin\Omega\cos\omega\cos i) + s_y(\sin\Omega\sin\omega - \cos\Omega\cos\omega\cos i) - s_z\cos\omega\sin i], \quad (10b)$$

$$\left\langle\frac{di}{dt}\right\rangle_{RP} = \frac{\alpha e}{(1-e^2)^{1/2}}(s_x\sin\Omega\cos\omega\sin i - s_y\cos\Omega\cos\omega\sin i + s_z\cos\omega\cos i), \quad (10c)$$

$$\left\langle\frac{d\Omega}{dt}\right\rangle_{RP} = \frac{\alpha e}{(1-e^2)^{1/2}}(s_x\sin\Omega\sin\omega - s_y\cos\Omega\sin\omega + s_z\sin\omega\cot i), \quad (10d)$$

$$\left\langle\frac{d\omega}{dt}\right\rangle_{RP} = \frac{\alpha(1-e^2)^{1/2}}{e}[s_x(\cos\Omega\cos\omega - \sin\Omega\sin\omega\cos i) + s_y(\sin\Omega\cos\omega + \cos\Omega\sin\omega\cos i) + s_z\sin\omega\sin i] - \cos i\left\langle\frac{d\Omega}{dt}\right\rangle_{RP}, \quad (10e)$$

$$\left\langle\frac{dM}{dt} - n\right\rangle_{RP} = -\frac{\alpha(1+e^2)}{e}[s_x(\cos\Omega\cos\omega - \sin\Omega\sin\omega\cos i) + s_y(\sin\Omega\cos\omega + \cos\Omega\sin\omega\cos i) + s_z\sin\omega\sin i]. \quad (10f)$$

Here $2\alpha/(3n) = \beta M_\odot a^2/(M_p R^2)$ is the ratio of the radiation force to the planet's gravity at a given semimajor axis. In terms of previous expressions $\alpha = 3/(2\tau_0)$ in Chamberlain's (1979) notation and $\alpha(1-e^2)^{1/2} = 3HF/(2m\mu)$ in Burns *et al.*'s (1979) notation. Eqs. (10a–f) are fully three-dimensional, valid for all eccentricities and inclinations.

It remains only to determine the coefficients s_x, s_y, and s_z. Imagine a rotating ecliptic coordinate system such that the Sun remains fixed along the x_R-axis. In general, at time $t = 0$, the Sun is located at an angle δ from the inertial reference direction in Fig. 2. To find the coordinates of a unit vector pointing toward the Sun in the equatorial frame, we apply two rotations; first a rotation of $-n_\odot t - \delta$ around the normal to the ecliptic back to the mutual node, then a rotation around the inertial direction by minus the obliquity to align the reference planes. In matrix notation, the transformation is

$$\hat{\mathbf{s}} = R_x(-\gamma)R_z(-n_\odot t - \delta)\hat{\mathbf{x}}_R, \quad (11)$$

where $R_x(\theta)$ and $R_z(\theta)$ are rotation matrices around the x and z axes, respectively (see Danby 1988, p. 425). Performing the multiplication, we find that

$$s_x = \cos(n_\odot t + \delta), \quad (12a)$$

$$s_y = \cos\gamma\sin(n_\odot t + \delta), \quad (12b)$$

and

$$s_z = \sin\gamma \sin(n_\odot t + \delta). \tag{12c}$$

Note that for $\gamma = 0$, $n_\odot = 0$, $\delta = 0$, we have $s_x = 1$, $s_y = s_z = 0$, and Eqs. (10a–e) reduce to those of Burns *et al.* (1979) or Chamberlain (1979). Mignard's (1982) equations are obtained after a little trigonometry, by letting $\gamma = 0$, $\delta = 0$, and employing the transformation $\Omega = \Omega_R + n_\odot t$. Here Ω_R is Mignard's longitude of the nodes which differs from Ω because the former is measured from a direction that rotates at an angular speed $n_\odot$. With a little trigonometry, we find that Eqs. (10a–f and 12a–c) are also in agreement with expressions derived independently by Smyth and Marconi (1993).

We have derived Eqs. (12a–c) last to emphasize the fact that orbit-averaging can be performed for arbitrary s_x, s_y, and s_z as long as their time dependence is slow compared to the particle's orbital period. For example, we could easily treat the problem of motion around a planet which orbits the Sun on an elliptical path by simply replacing the argument in the R_z rotation matrix in Eq. (11) by an expression valid for the Sun's nonuniform rate. Of course, in such a case it would also be necessary to add a time dependence to α to allow for the more important fact that radiation pressure weakens as the planet moves away from the Sun (*cf.* Hamilton and Burns 1992).

4. ELECTROMAGNETIC FORCES

4.1. General Remarks

The rings and small satellites of the outer planets lie close to their primaries in environments characterized by swarms of energetic charged particles trapped by strong magnetic fields. Immersed in this sea of particles, a dust grain quickly acquires an electric charge by a number of mechanisms (Goertz 1989), the most important of which are the electron and ion charging that occur as the grain sweeps up these gyrating particles. Uncharged dust grains are impacted by electrons more frequently than by ions because the thermal speed of the former far exceeds that of the latter—in essence, the electrons get to the grains before the ions do. As a grain becomes more negatively charged, it is able to electrostatically ward off some electrons while simultaneously attracting a comparable number of ions until a balance is attained (Burns and Schaffer 1989, their Fig. 1). For typical magnetospheric parameters and micrometer-sized grains, equilibrium is established in a fraction of an orbital period. The addition of other charging mechanisms, such as photoelectron currents and secondary electron emission, usually only perturbs the equilibrium grain charge, although for high secondary yields such processes can lead to multiple equilibria (Meyer-Vernet 1982). Finally, even the equilibrium charge may gradually change as the grain's orbit takes it into regions where plasma populations differ and as the grain's velocity relative to the plasma varies (*cf.* Burns and Schaffer 1989). Stochastic variations of the grain's charge, which are generally relatively small and occur swiftly, have little effect on orbital evolution (Schaffer and Burns 1993).

Despite the complexity of these charging mechanisms, it is often a good approximation to assume that the equilibrium charge on a grain is constant. Take, for example, the orbital elements displayed in Fig. 5 of Horanyi *et al.* (1992) which show an eccentric orbit that ranges from 1 out to 7 Saturnian radii. Although the relative velocity between the grain and the corotating plasma varies tremendously, changes in the equilibrium potential are limited to ±5%. This is in agreement with Fig. 1 of Burns and Schaffer (1989) which shows a weak dependence of the equilibrium potential on velocity. Potentially more serious are the fluctuations in a grain's charge caused by spatial and temporal variation in the density and temperature of the magnetospheric plasma. Because the plasma density in the E ring is relatively large, a grain's charge adjusts to its surroundings much more rapidly than the grain orbits the planet (Horanyi *et al.* 1992). If we make the reasonable assumption of cylindrically symmetric spatial variations in the plasma parameters, it can be shown, with the formalism to be introduced below, that the semimajor axis and eccentricity of the grain's orbit change in almost the same way as they do for a constant charge. Since the purpose of this section is to account for the first-order effects of the Lorentz force, henceforth we make the simplifying assumption of constant charge. We will return to comment further on the validity of this approximation for the specific case of Saturn's E ring.

Planetary magnetic fields are responsible not only for trapping the electrons and ions that charge up a dust grain, but also for the resulting orbital perturbations suffered by such grains. In the standard model, these fields are assumed to arise from two sources, currents interior to a given radial distance from the planet and currents exterior to this distance; connections between the regions are ignored. Because of the assumed lack of currents in the region of interest ($\mathbf{J} = \nabla \times \mathbf{B} = 0$), the magnetic field can be derived from a scalar magnetic potential Φ in analogy with the electric potential. The j,k component of the scalar magnetic potential in the frame rotating with the planet is given by the usual spherical harmonic expansion

$$\Phi_{j,k} = R_p \left(\frac{R_p}{r}\right)^{j+1} [g_{j,k}\cos(k\phi_R) + h_{j,k}\sin(k\phi_R)]P_j^k(\cos\theta), \tag{13}$$

where j is an integer ranging from zero to infinity, k is an integer ranging from zero to j, and $\phi_R = \phi - \Omega_p t$, with the

subscript R denoting the rotating coordinate system. Here θ and ϕ are the angular spherical coordinates defined in the nonrotating frame. The $g_{j,k}$ and $h_{j,k}$ are magnetic field coefficients with units of G which can be evaluated for each planet (for Saturn see Connerney *et al.* 1984; Schaffer and Burns 1992 tabulate values for the giant planets and give additional references). In Eq. (13) we have ignored the (usually small) contributions from the exterior currents; their effects can be readily included (Acuña *et al.* 1983) when necessary (*e.g.*, beyond a few planetary radii in the Jovian system). The Schmidt-normalized associated Legendre polynomials $P_j^k(x)$ are defined in terms of the regular Legendre polynomials; the relevant expressions can be found in Schaffer and Burns (1992). Finally, the magnetic field contribution from the j,k component of the potential is

$$\mathbf{B}_{j,k} = -\nabla\Phi_{j,k}, \tag{14}$$

while the total field in the rotating frame is obtained by summing all of the individual components

$$\mathbf{B} = \sum_{j=1}^{\infty}\sum_{k=0}^{j}\mathbf{B}_{j,k}. \tag{15}$$

Two ways exist to obtain the Lorentz force valid in a nonrotating frame centered on the planet. Although the methods give identical results, they are conceptually quite different and it is instructive to go through each argument. In the first method, we calculate the force in the rotating frame as $\mathbf{F}_{\rm EM} = q(\mathbf{v}_{\rm rel}/c \times \mathbf{B})$ with $\mathbf{v}_{\rm rel} = \mathbf{v} - (\Omega_{\rm p} \times \mathbf{r})$, where $\mathbf{v}_{\rm rel}$ is the orbital velocity of the dust grain relative to the rotating frame, $\mathbf{v}$ is its velocity relative to a nonrotating planetocentric coordinate system, $\Omega_{\rm p}$ is the spin vector of the planet, c is the speed of light, and q is the charge on the grain. Employing special relativity to transform the force back to the nonrotating frame, we find that it is unaltered to first-order in v/c and hence

$$\mathbf{F}_{\rm EM} = \frac{q}{c}\{[\mathbf{v} - (\Omega_{\rm p} \times \mathbf{r})] \times \mathbf{B}\}. \tag{16}$$

The preceding discussion makes it quite clear that the Lorentz force vanishes for an equatorial circular orbit at the synchronous distance: there the velocity relative to the magnetic field is zero and thus no force is present.

The second way to treat the problem is to transform the magnetic field from rotating coordinates to nonrotating ones before calculating the force. Utilizing special relativity again, we find that the magnetic field is unchanged (neglecting terms of order $\Omega_{\rm p} r/c \ll 1$), and that an electric field $\mathbf{E} = -(\Omega_{\rm p} \times \mathbf{r}) \times \mathbf{B}$ is present in the nonrotating frame. This is the so-called "corotational electric field" discussed by Burns and Schaffer (1989) among others. The Lorentz force is then calculated from $\mathbf{F}_{\rm EM} = q[\mathbf{E} + (\mathbf{v}/c \times \mathbf{B})]$ and Eq. (16) is obtained once more. This discussion highlights the role of the magnetic field; it illustrates that part of the Lorentz force does no work and, as we shall see, is less able to influence the orbital elements.

Although the magnetic field can be expressed as a gradient of a potential, the electromagnetic force, because of its velocity dependence, cannot. We are therefore unable to use the disturbing function approach that was applied to radiation pressure and instead must use Gauss' form of the planetary equations. These equations are given in orbital coordinates where the force at a particular point on the orbit is resolved into orthogonal components which are radial ($\hat{\mathbf{R}} = \hat{\mathbf{r}}$), normal to the orbit ($\hat{\mathbf{N}}$), and tangential to a circle in the orbital plane that passes through the point ($\hat{\mathbf{C}}$). The Lorentz force, Eq. (16), is written in equatorial spherical coordinates which are converted into the orbital coordinates by use of Eqs. (5)–(7) and the following expressions:

$$\hat{\theta} = -\frac{\cos i}{\sin\theta}\mathbf{N} - \frac{\sin i \cos u}{\sin\theta}\hat{\mathbf{C}}, \tag{17}$$

and

$$\hat{\phi} = -\frac{\sin i \cos u}{\sin\theta}\hat{\mathbf{N}} + \frac{\cos i}{\sin\theta}\mathbf{C}. \tag{18}$$

Carrying out the transformation and keeping track of all terms, we find that the normal, radial, and tangential components of the Lorentz acceleration can be represented as

$$N = \frac{q}{cm_{\rm g}}\left(-\frac{v_r B_\theta \sin i \cos u}{\sin\theta} + \frac{v_r B_\phi \cos i}{\sin\theta} - B_r v_C + B_r \Omega_{\rm p} r \cos i\right), \tag{19a}$$

$$R = \frac{q}{cm_{\rm g}}\left(-\frac{v_C B_\theta \cos i}{\sin\theta} - \frac{v_C B_\theta \sin i \cos u}{\sin\theta} + B_\theta \Omega_{\rm p} r \sin\theta\right), \tag{19b}$$

$$C = \frac{q}{cm_{\rm g}}\left(\frac{v_r B_\theta \cos i}{\sin\theta} + \frac{v_r B_\phi \sin i \cos u}{\sin\theta} + B_r \Omega_{\rm p} r \sin i \cos u\right), \tag{19c}$$

where v_r and v_C are the radial and circular parts of the velocity and the B_i are the appropriate magnetic field components. These three equations are valid for any magnetic field. Finally we need to express the radial and circular

velocity components of a Keplerian elliptical orbit in terms of the orbital elements; from conservation of orbital energy and angular momentum we have

$$v_r = \left(\frac{\mu}{a}\right)^{1/2} \frac{e \sin \nu}{(1-e^2)^{1/2}}, \tag{20a}$$

and

$$v_C = \left(\frac{\mu}{a}\right)^{1/2} \frac{1 + e \cos \nu}{(1-e^2)^{1/2}}. \tag{20b}$$

4.2. The Aligned Dipole

We begin by discussing the axisymmetric ($k = 0$) terms in the magnetic field expansion given by Eqs. (13)–(15) as they have no time dependence and can be readily orbit-averaged. Of these, the $j = 1$ term is the strongest so we focus on it first. The magnetic field produced by this $g_{1,0}$ term is a spin-axis aligned dipole which has the following components:

$$B_r = 2g_{1,0}\left(\frac{R_p}{r}\right)^3 \cos\theta, \tag{21a}$$

$$B_\theta = g_{1,0}\left(\frac{R_p}{r}\right)^3 \sin\theta, \tag{21b}$$

$$B_\phi = 0. \tag{21c}$$

For convenience, and in analogy with Eq. (4), we define a dimensionless parameter, L, as a rough measure of the strength of the electromagnetic force relative to the planet's gravity. We take the $g_{1,0}$ term of the magnetic field given in Eqs. (21a–c), evaluate Eq. (16) in the equatorial plane with $\mathbf{v} = 0$, and divide by the planet's gravitational force (note this is similar to the parameter ε defined by Schaffer and Burns (1987)). The result is

$$L = \frac{q g_{1,0} R_p^2 \Omega_p}{c \mu m_g}. \tag{22}$$

Inserting the force resulting from Eqs. (21a–c) into the planetary perturbation equations and performing the time-averages we obtain

$$\left\langle \frac{da}{dt} \right\rangle_{g_{1,0}} = 0, \tag{23a}$$

$$\left\langle \frac{de}{dt} \right\rangle_{g_{1,0}} = -\frac{nL}{4} e(1-e^2)^{1/2} \sin^2 i \sin(2\omega), \tag{23b}$$

$$\left\langle \frac{di}{dt} \right\rangle_{g_{1,0}} = \frac{nL}{4(1-e^2)^{1/2}} e^2 \sin i \cos i \sin(2\omega), \tag{23c}$$

$$\left\langle \frac{d\Omega}{dt} \right\rangle_{g_{1,0}} = \frac{nL}{(1-e^2)^{1/2}} \left[\cos i - \frac{1}{(1-e^2)} \left(\frac{n}{\Omega_p}\right) \right], \tag{23d}$$

$$\left\langle \frac{d\omega}{dt} \right\rangle_{g_{1,0}} = \frac{nL}{(1-e^2)^{1/2}} \left[-\cos^2 i + \frac{3\cos i}{(1-e^2)} \left(\frac{n}{\Omega_p}\right) \right], \tag{23e}$$

$$\left\langle \frac{dM}{dt} - n \right\rangle_{g_{1,0}} = -2nL. \tag{23f}$$

These expressions have been simplified from exact formulae by dropping terms of high order in e and i. Nevertheless, Eqs. (23a–f) are quite accurate even for very large inclinations and eccentricities as we shall soon see.

The electromagnetic force, like radiation pressure, makes nonzero contributions to variations in the eccentricity and inclination but these contributions depend on powers of $\sin i$ and e; they are therefore quite small unless the orbit under consideration is both highly eccentric and significantly inclined. Thus, at least for small inclinations and eccentricities, the effect of the planet's dipolar magnetic field is not unlike that of J_2 (the planet's quadrupole gravitational field) since both forces primarily cause precession. This crude similarity should not be surprising since, at least near the equator plane, both forces have strengths that diminish rapidly with distance and directions that are predominantly radial. For electromagnetism, the nodal and apsidal precession rates are dependent on inclination, eccentricity, and the semimajor axis as are their J_2 counterparts. Unlike the gravitational case, however, the electromagnetic rates vary considerably relative to one another for circular orbits of different sizes near the equatorial plane (compare Eqs. [23d,e] with [2d,e]). Close to synchronous orbit ($n = \Omega_p$), for example, the nodal rate vanishes, while the apsidal rate is zero further from the planet near the place where $3n = \Omega_p$. Incidentally, as synchronous orbit is approached in the limit ($n \to \Omega_p$, $e \to 0$, $i \to 0$), the Lorentz force vanishes as does the nodal rate, but the pericenter rate does not. How can a force which is zero all along an orbit cause orbital evolution? The solution to this apparent paradox is, of course, that it does not; a circular orbit has no unique pericenter so the fact that the rate of change of an ill-defined angle fails to vanish is unimportant. For small eccentricities, pericenter exists, the Lorentz force is nonzero, and Eq. (23e) gives the correct precession rate.

4.3. The Aligned Quadrupole

As in the gravitational case, inclusion of the higher-order axisymmetric ($k = 0$) terms in the magnetic field expansion requires that the lower-order terms be treated more carefully (*i.e.*, taken out to the next order in L), a task that rapidly increases in algebraic complexity. For

gravity, a treatment including just the J_2 term is a good approximation because J_3 and the other odd harmonics are all exceedingly small for planets, and because the fields produced by the larger, even harmonics fall off very quickly with increasing distance. Accordingly, we might hope that higher-order symmetric terms in the electromagnetic expansion could be ignored as well. We find, however, that the axisymmetric quadrupole has a nontrivial influence on orbital dynamics; its importance can be easily understood by noting that near the equator, the radial component of the dipole magnetic field is small (of order i). In contrast, the quadrupole field is primarily radial and its magnitude actually exceeds the radial dipolar field for orbits with small inclinations. When crossed into a transverse velocity, the radial field produces a strong normal force which perturbs the inclination, node, and pericenter; hence we expect that quadrupole effects will be important for these elements. Further expansion to include the symmetric octupole and higher $k = 0$ terms is often unnecessary, as the radial and theta components of the combined dipole and quadrupole magnetic field usually dominate contributions from higher-order terms.

Rather than repeating the derivations of Section 4.2 for the symmetric quadrupole term (an arduous task!), we treat only the case of small inclinations, which is of the most interest for planetary applications. For inclinations smaller than 30°, the theta component of the magnetic field is dominated by the dipole term and so we ignore the small quadrupole contributions to that component. The radial component of the quadrupole field,

$$B_r = \frac{3}{2} g_{2,0} \left(\frac{R_p}{r}\right)^4 (3\cos^2\theta - 1), \tag{24}$$

however, is important. The largest effect of the radial quadrupole field on a slightly inclined orbit is to produce a normal force. Consequently, we ignore Eqs. (19b,c) and consider only Eq. (19a). This force affects only the inclination, node, and pericenter derivatives. The first two terms of Eq. (19a) are identically zero because we have ignored the theta component of the quadrupole field and there is no phi component. Furthermore, it turns out that the final term also contributes nothing. Performing the much simplified averaging calculation, we obtain

$$\left\langle \frac{di}{dt} \right\rangle_{g_{2,0}} \approx \frac{3}{2} nL \left(\frac{g_{2,0}}{g_{1,0}}\right)\left(\frac{R_p}{a}\right)\left(\frac{n}{\Omega_p}\right) \frac{e\cos\omega}{(1-e^2)^{5/2}}, \tag{25c}$$

$$\left\langle \frac{d\Omega}{dt} \right\rangle_{g_{2,0}} \approx \frac{\tan\omega}{\sin i} \left\langle \frac{di}{dt} \right\rangle_{g_{2,0}}, \tag{25d}$$

$$\left\langle \frac{d\omega}{dt} \right\rangle_{g_{2,0}} \approx -\cos i \left\langle \frac{d\Omega}{dt} \right\rangle_{g_{2,0}}, \tag{25e}$$

where approximation signs have been used instead of equals signs to remind the reader that these equations represent only part of the quadrupole perturbations, albeit the most important contributions for low inclination orbits. In this limit, additional quadrupole perturbations are insignificant when compared to the effects of the aligned dipole.

Note that, with a little manipulation, the form of Eqs. (25c–e) is identical to the s_z component of the radiation pressure equations (Eqs. 10c–e). This occurs because both sets of equations arise from small, nearly constant vertical forces being applied to an orbit; we take advantage of this similarity in Section 5 to follow. The sin i in the denominators of Eqs. (10d) and (25d) simply expresses the fact that, for low inclinations, the orbital node is poorly defined and small perturbations can force large changes in that element.

4.4. Asymmetric Terms

Up to now, we have ignored the nonaxisymmetric ($k \neq 0$) terms in the magnetic field expansion; this is a good approximation for the almost perfectly aligned Saturnian field (Connerney *et al.* 1984), but not for the magnetic fields of the other giant planets. Although we will apply our results only to Saturn in this paper, the expressions devied above are general and are valid for all of the planets. Thus nonaxisymmetric magnetic field terms merit a brief discussion. First of all, we note that asymmetric terms are more difficult to treat than the symmetric ones since the planet's rotation causes the field's orientation to change rapidly. Typically, a planet's spin period is comparable to the orbital period of an inner orbit; for this type of orbit there is not a unique timespan over which to average. In contrast, distant orbits have periods that are so long that we can average the magnetic field first over a single spin period and then over the orbital motion. Following this procedure, we find that all of the nonaxisymmetric terms in Eq. (13) average to zero (*i.e.*, they give no contribution to orbital evolution in this limit).

Encouraged by this result, we might be tempted to ignore the effects of the nonaxisymmetric terms even close to the planet, arguing that they will only induce small periodic oscillations. For most orbits this is true, but at specific locations orbital and spin frequencies are commensurate and the averaging process is invalid (*cf.* Schaffer and Burns 1992, Burns *et al.* 1985). These "Lorentz" resonances can be treated by isolating the commensurate terms in Eqs. (19a–c) for use in the planetary equations, but for now we ignore the nonaxisymmetric terms and accept the fact that the orbit-averaged equations derived in this section will not be valid near resonant locations. We have analyzed these Lorentz resonances and will discuss them in a future publication (Hamilton and Burns 1993a).

5. COUPLED PERTURBATIONS

In the circumplanetary environment, all three perturbation forces discussed above (higher-order gravity, the electromagnetic force, and radiation pressure) conspire to perturb the orbits of micrometer-sized dust grains. Since the forces are generally small, the orbit-averaged equations derived in the previous sections can be simply summed to account for the cumulative effect of all perturbations,

$$\left\langle \frac{d\Psi}{dt} \right\rangle_{\text{total}} = \sum_j \left\langle \frac{d\Psi}{dt} \right\rangle_j, \tag{26}$$

where Ψ is any of the six osculating orbital elements. The resulting expressions are cumbersome, but several hundred times faster to numerically integrate than their Newtonian counterparts. In addition, the output of the Newtonian equations (vector position and velocity) must be translated into osculating orbital elements. As a demonstration of the validity of our derivations, we compare numerical integrations of the Newtonian (Fig. 3a) and orbit-averaged (Fig. 3b) equations for a 1-μm grain charged to -5.6 V, approximately the potential expected in the Saturnian environment (Horanyi *et al.* 1992, Fig. 1). The initial conditions in both cases are appropriate for a grain launched from the moon Enceladus on an initially circular coplanar orbit at $3.95R_p$. Plotted are the five osculating orbital elements and the *solar angle* $\phi_\odot$ (defined below). All six panels of the two plots agree quite well which reassures us that the approximations made in the previous sections are valid.

The most notable difference between Figs. 3a and b appears in the semimajor axis traces; in the first figure, the semimajor axis displays a peculiar "fuzziness," while no evolution whatsoever is apparent in the second. The discrepancy is due to effects that occur during a single orbital period; in Fig. 3a these effects are clearly visible, while in Fig. 3b they do not exist because they have been averaged out. These short period terms arise when the vector position and velocity are translated into the osculating orbital elements; in the presence of perturbations, the values of the elements depend on the point along an orbit at which they are calculated. The difference in these values over a single orbit is first-order in the small dimensionless quantities J_2, α/n, and L, and the oscillations in osculating semimajor axis are greater for larger eccentricities as can be readily seen in the plot. By noting the value of a in Fig. 3a at points where $e \approx 0$, however, we see that no long term change occurs in the semimajor axis, in agreement with Fig. 3b. The fact that the rapid and sometimes discontinuous changes in ω and Ω that occur at low e and i are not perfectly reproduced (see Figs. 3a and 3b at $t \sim 8$ years for example) is unimportant since these variables become singular as e and i, respectively, tend toward zero.

The agreement between Figs. 3a and b also encourages qualitative and quantitative descriptions of evolution based on the orbit-averaged equations. To assist this endeavor, we write out Eq. (26) explicitly. As noted above, most sources for circumplanetary dust are thought to be the small moons and rings orbiting close to their planet; these objects move in nearly circular orbits in the equatorial plane. While radiation pressure can cause eccentricities of some initially circular orbits to grow quite large (Horanyi *et al.* 1992), it is often difficult for grains to attain orbits significantly inclined to the equatorial plane. This supposition holds for orbits close to the planet and away from the Lorentz resonant locations. A useful limit for analytic work, therefore, is that of nearly equatorial orbits. We keep only the leading terms in $\sin i$ for each element and also take $i < \gamma$, which is a reasonable assumption in most cases (Jupiter is a possible exception as $\gamma \sim 3°$). Additionally, we assume that $\gamma \lesssim 30°$ so that $\cos \gamma \approx 1$; this, of course, is not a good approximation for Uranus with $\gamma \approx 98°$! Using Eq. (26) to sum the effects of all of the forces discussed in the previous sections, we find, with the help of some trigonometric identities, that

$$\left\langle \frac{da}{dt} \right\rangle = 0, \tag{27a}$$

$$\left\langle \frac{de}{dt} \right\rangle = \alpha(1 - e^2)^{1/2} \sin \phi_\odot, \tag{27b}$$

$$\left\langle \frac{di}{dt} \right\rangle = Z \cos \omega, \tag{27c}$$

$$\left\langle \frac{d\Omega}{dt} \right\rangle = Z \frac{\sin \omega}{\sin i} + \dot{\Omega}_{xy}, \tag{27d}$$

and

$$\left\langle \frac{d\omega}{dt} \right\rangle = -Z \frac{\sin \omega}{\sin i} + \dot{\omega}_{xy}. \tag{27e}$$

Here

$$\phi_\odot \equiv \Omega + \omega - n_\odot t - \delta \tag{28}$$

is the *solar angle*, approximately the angular difference between the longitudes of the Sun and the orbit's pericenter measured in the equatorial plane; the change in this angle is given by

$$\dot{\phi}_\odot = \dot{\Omega}_{xy} + \dot{\omega}_{xy} - n_\odot. \tag{29}$$

The precession rates arising from oblateness, electromagnetic, and radiation forces (excluding the terms proportional to Z, defined immediately below) are

$$\dot{\Omega}_{xy} = -\frac{3nJ_2R_p^2}{2a^2(1-e^2)^2} + \frac{nL}{(1-e^2)^{3/2}}\left(1 - e^2 - \frac{n}{\Omega_p}\right) \quad (30)$$

and

$$\dot{\omega}_{xy} = \frac{3nJ_2R_p^2}{a^2(1-e^2)^2} - \frac{nL}{(1-e^2)^{3/2}}\left(1 - e^2 - \frac{3n}{\Omega_p}\right) + \frac{\alpha(1-e^2)^{1/2}\cos\phi_\odot}{e}; \quad (31)$$

the Z terms are excluded for reasons that will become apparent in the following sections. Finally, the quantity

$$Z = \frac{e}{(1-e^2)^{1/2}}\left[\alpha s_z + \frac{3}{2(1-e^2)^2} nL\left(\frac{g_{2,0}}{g_{1,0}}\right)\left(\frac{R_p}{a}\right)\left(\frac{n}{\Omega_p}\right)\right], \quad (32)$$

represents the contributions of the two vertical forces in the problem: the out-of-plane component of radiation pressure and the force arising from the aligned quadrupole field. These two forces are small and do not cause substantial orbital evolution; note that the terms proportional to Z in Eqs. (27d,e) are equal and opposite so that for small i, the absolute position of pericenter $\Omega + \omega$ is unaltered. Nevertheless, the forces are important because they influence the vertical extent of an orbit, as will be discussed in greater detail below.

The presence of J_2, L, and α in all of the above expressions indicate the effects of oblateness, electromagnetism, and radiation pressure, respectively; Eq. (27b), for example, shows that eccentricity is driven solely by radiation pressure. Additional approximations to the set of equations (27a–e) can be made for specific situations. For example, we can drop the electromagnetic terms for orbits around bodies with insignificant magnetic fields (Venus, Mars, Pluto, asteroids, and comets) or for small uncharged objects (atoms and molecules) around any planet. In the latter case, Eq. (4) would need to be altered since geometrical optics is not valid for atoms and molecules (*cf.* Smyth and Marconi 1993).

6. APPLICATION TO THE SATURNIAN E RING

6.1. Observations and Previous Work

We now apply these low-inclination results to describe the orbital evolution of particles in Saturn's E ring. This ring extends over a broad radial range from $<3R_p$ out to $8R_p$ crossing the orbits of several satellites; its strong peak in optical depth near the orbit of Enceladus has caused many to argue that this moon is the likely source of E ring grains. Additionally, in a thorough analysis of the ground-based observations (*e.g.*, Baum *et al.* 1981, Larson *et al.* 1981) and Voyager images at a variety of phase angles, Showalter *et al.* (1991) found that the scattering properties of the E ring are consistent with a monosize distribution of grains with radii 1 ($\pm$0.3) μm. Because of the ring's low optical depth, Horanyi *et al.* (1992) studied single particle orbital dynamics of grains launched from Enceladus and discovered that a cancellation in the orbital precession rates, occurring for dust grains near a micron in radius, allows radiation pressure to force initially circular orbits to become highly eccentric, thereby driving material across a large radial range. The model explains how this material can rapidly spread both inside and outside of Enceladus' orbit, emphasizes the dynamical importance of one micron-sized grains, and predicts the vertical shape of the E ring quite well. Nevertheless, a few problems with the Horanyi *et al.* (1992) model remain, most notably:

(1) As seen from Earth during ring-plane crossings, the E ring extends further from Saturn than predicted by the model.

(2) The predicted vertical extent of the E ring is 10 times less than that observed.

Hamilton and Burns (1993b) suggest that other satellites, most notably Tethys, provide additional sources for E ring material. In the latter model, high-velocity impacts of E ring grains into Saturnian satellites blast debris off these moons into circumplanetary orbits. The model naturally explains why the peak in the E ring's optical depth occurs at Enceladus rather than at one of the other embedded satellites and predicts a size distribution that is likely to be consistent with the observations. The problems listed above are alleviated, but not fully solved, by adding the other Saturnian satellites as supplementary E ring sources. In the following two sections, we use the equations derived above to more thoroughly understand the dynamics of E ring orbits, thereby gaining insight into the ring's three dimensional structure. Our improved understanding of the ring's azimuthal and vertical profile suggests solutions to problems (1) and (2), respectively.

6.2. Azimuthal Structure: Eccentricity and Solar Angle

The orbital perturbation responsible for most of the E ring's structure is the large, almost periodic variation in the eccentricity displayed in Figs. 3a and b. In contrast, the semimajor axis remains essentially constant and the inclination stays small. Due to the latter fact, substantial variations in Ω and ω do little to change the orbit. Furthermore, since the governing equation (Eq. 27b) for eccentricity in this low inclination limit depends only on the solar angle and the eccentricity itself, these two variables can be decoupled from the rest. Accordingly we discuss

the eccentricity and the solar angle in this section and the elements i, Ω, and ω in the next.

Ideally, we would like to find an exact solution for Eqs. (27b) and (29) but, due to the presence of nonlinear $1 - e^2$ terms, we have been unable to do so. By contrast, for small eccentricities $\dot{\phi}_\odot$ is nearly a constant, and a solution, in which the eccentricity varies sinusoidally, can be easily found (Burns *et al.* 1979; Horanyi *et al.* 1992). In the present case, however, we are interested in highly eccentric orbirts and so are forced to content ourselves with a qualitative description of the orbital evolution based on these two equations. First, as predicted by Eq. (27b) and seen in Fig. 3, the eccentricity always grows when $0° \lesssim \phi_\odot \lesssim 180°$ and shrinks when $180° \lesssim \phi_\odot \lesssim 360°$. When $\dot{\phi}_\odot \approx 0$, $\phi_\odot$ in Eq. (27b) remains nearly constant, the elliptical orbit keeps a given orientation with respect to the Sun, and the eccentricity changes monotonically. This situation occurs, with expected plasma parameters at the distance of Enceladus, for E ring grains about 1 μm in radius (Horanyi *et al.* 1992). In the low eccentricity solution considered by these authors, an exact cancellation of the precession rates with a associated permanent growth of eccentricity is possible but, as seen in Eqs. (30) and (31), the rates actually depend on different powers of $1 - e^2$, which causes an imperfect cancellation as the eccentricity varies. At large e, these nonlnear effects are important and significantly influence the azimuthal structure of the ring.

In order to study the nonlinear effects, we must first understand the simple case when these terms are absent; this situation is approximated in Fig. 3 where e^2 is always relatively small. As Fig. 3 shows, at $t = 0$ the solar angle $\phi_\odot$ is immediately driven to 90° by radiation pressure; this occurs because, for small eccentricities, the final term in Eq. (31) dominates $\dot{\phi}_\odot$. After the eccentricity rises slightly, the final term is less important so that the solar angle *regresses* continually from $t = 0$ to $t \approx 8.5$ years under the gravitational and electromagnetic terms in Eqs. (30) and (31); in this example, the regression rate is nearly uniform because, for these relatively low eccentricities, nonlinear terms are small. The vertical "jumps" in $\phi_\odot$, an example of which occurs at $t = 5$ years in Fig. 3, are due simply to the fact that the angle is plotted modulo 360°. As soon as the solar angle crosses zero, the eccentricity begins decreasing until eventually it is sufficiently small that the final term in Eq. (31) dominates again. As before, this term attempts to drive $\phi_\odot$ to 90° causing the angle to become positive and the eccentricity to increase. The cycle repeats almost periodically with departures from periodicity arising from the sensitive dependence of $\dot{\phi}_\odot$ on e.

Because of the coupling between e and the solar angle, the largest eccentricities in Fig. 3 are attained when the pericenter of the orbit is pointed toward the Sun ($\phi_\odot = 0°$). At this time, apocenter is directed away from the Sun and, accordingly, particles reach their maximum distance from the planet in this direction ($r = a(1 + e)$—see Fig. 1a). Thus, if the E ring were composed solely of such particles, it would be asymmetric in azimuth, extending further in the antisolar direction than in the solar direction. A less negatively charged grain or, alternatively, a slightly larger particle, would have an initially *precessing* solar angle so that the maximum eccentricity would occur when the apocenter of the orbit points toward the Sun ($\phi_\odot = 180°$). Since the true E ring is likely composed of an ensemble of grains with slightly different sizes, shapes, and/or charges, it will probably include both precessing and regressing orbits with some apocenters pointing toward and others away from the Sun. This ensemble predicts that the E ring will be shaped like a Saturn-centered ellipse, extending to equal distances in the solar and antisolar directions and less far in the perpendicular directions. Such a distribution would minimize the rings apparent radial extent as viewed from Earth. This case, discussed by Horanyi *et al.*(1992), does not include the effects of $1 - e^2$ terms.

To demonstrate how larger eccentricities produce nonlinear effects, we consider the orbital evolution of a 1-μm grain charged to −5.4 V (as opposed to −5.6 V for Fig. 3); all other initial conditions as well as the operating forces remain unchanged. The resulting orbital evolution, obtained from numerical integrations of Eqs. (27a–e), is displayed in Fig. 4. The only difference between the two cases is the slightly altered grain charge, yet striking dissimilarities are apparent in both the eccentricity and solar angle traces. In Fig. 4, the solar angle initially regresses as it does in Fig. 3, but the regression is slightly less rapid; this allows the eccentricity to grow large enough to reverse the sign of $\dot{\phi}_\odot$ before the solar angle dips below zero. As a result $\sin \phi_\odot$ is larger for a longer period of time, permitting the eccentricity to increase substantially. The augmented eccentricity causes the solar angle to *precess* through 180°, at which point the eccentricity finally begins to decrease and a cycle similar to that discussed above is established. Azimuthal asymmetry arises because the stronger $1 - e^2$ dependence of the gravitational precession terms in Eqs. (30) and (31) causes the orbit to *precess* for large e which always leads to a maximum extension in the solar direction ($\phi_\odot = 180°$). Although for this orbit, e is large enough that the grain would actually be lost to the main Saturnian ring system (Horanyi *et al.* 1992 show that $e = 0.65$ is the largest eccentricity that a grain from Enceladus can attain), the orbital evolution displayed here is typical for a large range of similar initial conditions.

We now summarize the relevance of these results to the E ring problem. Consider an ensemble of grains with slightly different sizes and voltages, but all launched from Enceladus on initially circular orbits. A fraction of the

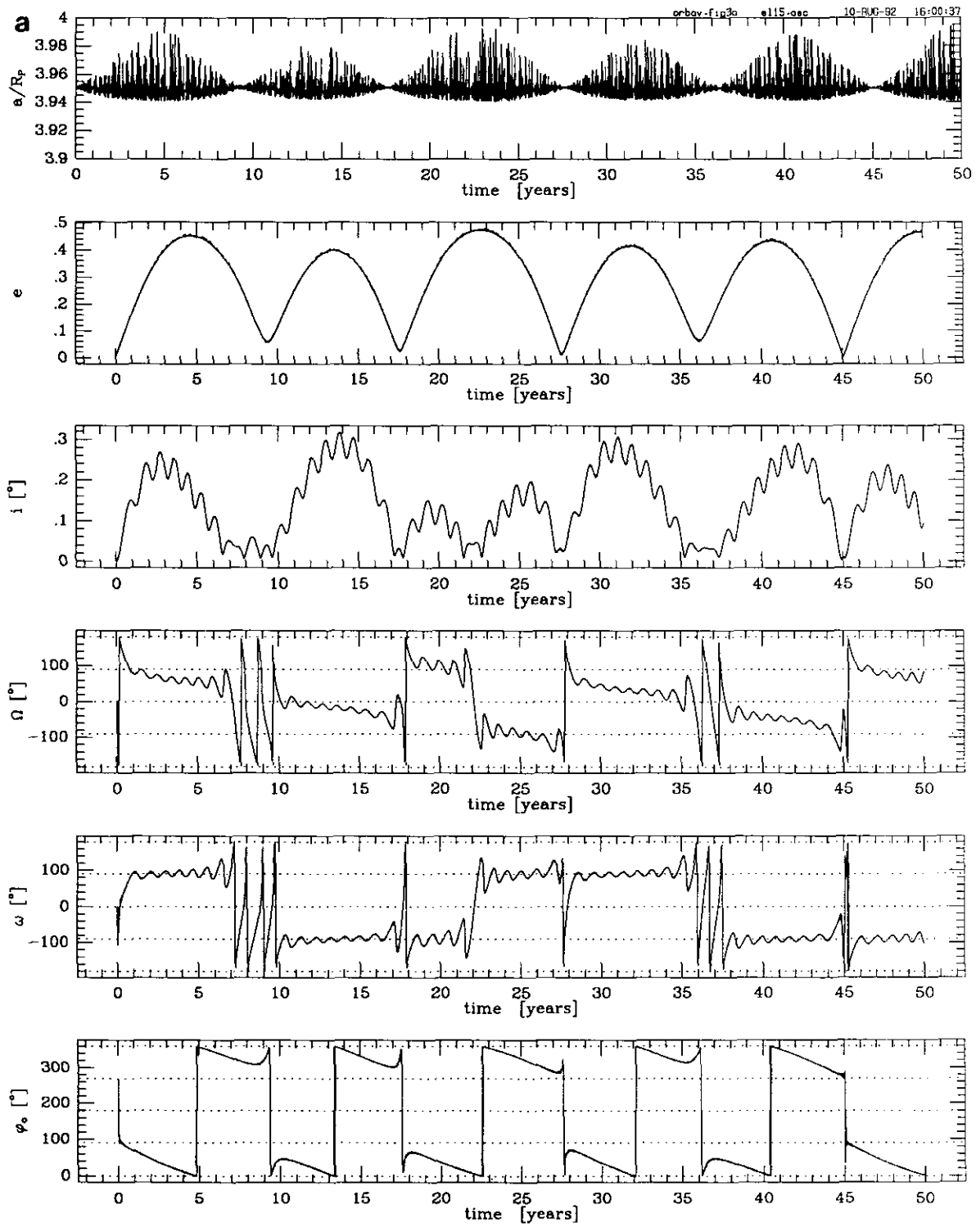

FIG. 3. Osculating orbital elements plotted against time from integrations of the (a) full Newtonian and (b) orbit-averaged equations of motion. Both integrations used the same initial conditions: a spherical grain 1 μm in radius ($\rho_g = 1 g/cm^3$, $Q_{pr} = 1$) charged to a potential of -5.6 V initially released from Enceladus at $3.95R_p$ on a circular Keplerian orbit in the equatorial plane. Forces operating on the orbit include the monopole and J_2 components of the gravity field, radiation pressure (no shadowing), and the Lorentz force from an aligned dipole. The agreement between the two methods is very good and is discussed further in the text. Other values of interest are the three dimensionless parameters $J_2 = 0.01667$, $\alpha/n = 0.00012$, $L = -0.00295$; the ratio $n/\Omega_p = 0.32439$, and the initial precession rates, as given by Eqs. (30) and (31), $\dot{\Omega}_{xy}(e \sim 0) = -345°$/year and $\dot{\omega}_{xy}(e \sim 0, \phi_\odot = 90°) = 315°$/year. The difference between the two rates is roughly the initial slope of the solar angle trace in the sixth panel.

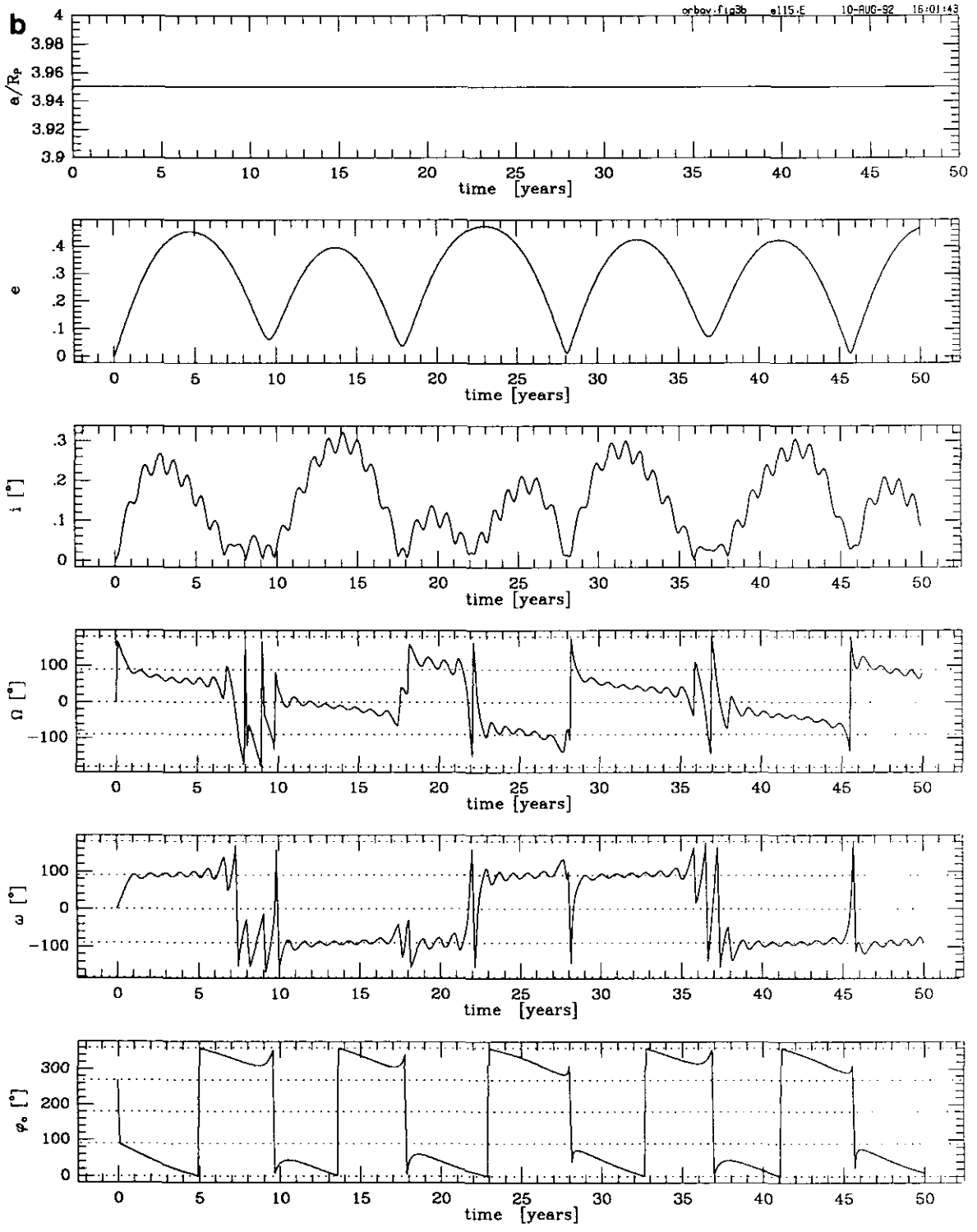

FIG. 3—*Continued*

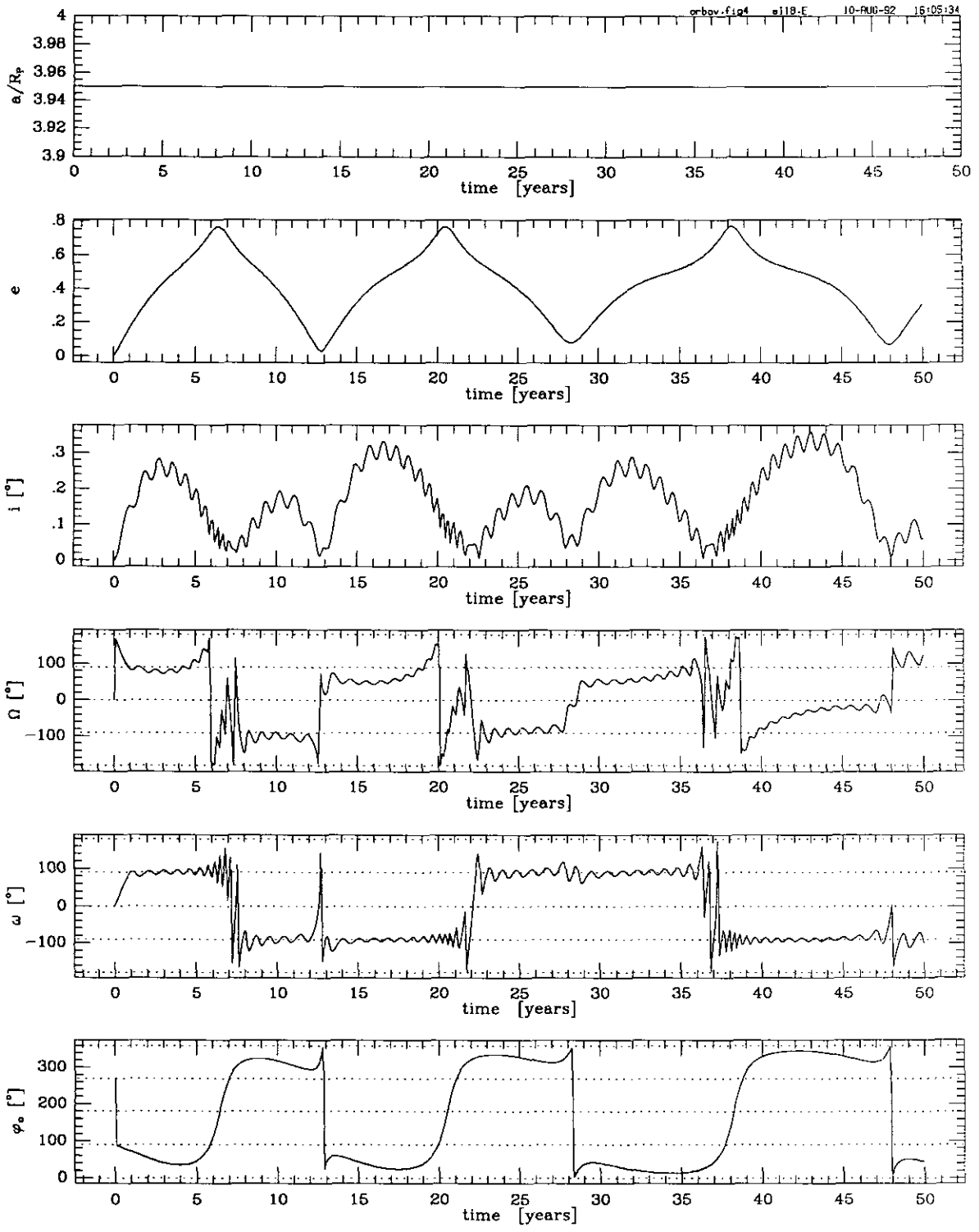

FIG. 4. Osculating orbital elements plotted against time from integrations of the orbit-averaged equations of motion; these agree well with full Newtonian integrations (not shown). The same forces operating in Fig. 3 are present here, and the initial conditions are identical to those in Fig. 3 except the grain's voltage has been changed slightly to −5.4 V. This small change in the voltage decreases the strength of the electromagnetic force ($L = -0.00284$) which in turn, changes the precession rates to $\dot{\Omega}_{\gamma\gamma}(e \sim 0) = -338°$/year and $\dot{\omega}_{\gamma\gamma}(e \sim 0, \phi_\odot = 90°) = 315°$/year; all other quantities retain the values noted in Fig. 3's caption. These slightly different precession rates drastically affect the eccentricity history.

grains in this ensemble will have $e_{max} \lesssim 0.4$; these will be relatively uninfluenced by the nonlinear $1 - e^2$ terms and will lead to the "Saturn-centered ellipse" discussed above. In addition, however, our ensemble will contain grains that achieve large eccentricities. These particles all precess eventually (the orbit in Fig. 3 almost attains the largest eccentricity possible with a strictly regressing solar angle), and so the maximum eccentricity always occurs when the apocenter is pointed toward the Sun. Furthermore, because precession is rapid for very large eccentricities, the most elongated orbits sweep through a large range of pericenter angles (see the solar angle and eccentricity panels between $t = 6$ and $t = 7$ years in Fig. 4), resulting in distant particles in all directions on the sunward side of Saturn. Since the real ring contains both dynamical classes, an Enceladus-derived E ring might be expected to extend ~1.2 times as far in the solar and perpendicular directions as in the antisolar direction. In contrast to the Horanyi *et al.* (1992) model, this distribution displays nearly its full radial extent when viewed from Earth.

The above discussion explicitly assumes that the charge on a grain remains constant throughout its orbital evolution. Could a varying particle charge disrupt the behavior seen here? Realistically, small rapid fluctuations in a grain's voltage occur as the grain's position in the magnetosphere (where plasma densities and temperatures might vary) and its velocity relative to the plasma change. A delay in the response of the grain's voltage to local conditions can affect long term evolution of semimajor axes (Burns and Schaffer 1989), but over the short times considered here, this process is unlikely to be important. Because the charge fluctuations are fast compared to the orbital period, however, they should be treated before averaging the perturbation equations over an orbit. As argued above, this will not seriously influence the orbital semimajor axis and eccentricity. The inclination and precession equations, however, are more strongly affected. A difference in the inclination equation only adjusts the magnitude of Z (Eq. (32)), however, which does not seriously alter the behavior of Eqs. (23c–e). Slightly different electromagnetic precession rates would still cancel the gravitational rates, although at a minutely different grain size. Most importantly, the $1 - e^2$ dependence of the electromagnetic precession rate could be changed significantly (exponent < -2). In this case, the nonlinear effect that favors an E ring with a minimum extension in the antisolar direction would be reversed. The E ring would then have its small dimension in the solar direction. In any case, an asymmetry of some sort is likely to persist.

Finally we point out that the surface brightness of the E ring depends not only on these dynamic considerations but perhaps even more on the detailed distribution of particle sizes and shapes present in the E ring. This distribution determines the number of grains in each of the dynamical classes discussed two paragraphs back. If orbits with lower eccentricities (Fig. 4) are most prevalent, for instance, then the surface brightness will be dominated by the "Saturn-centered ellipse." Whatever the size distribution though, the E ring's surface brightness should display measurable azimuthal asymmetry.

6.3. Vertical Structure: Inclination, Node, and Pericenter

Having completed our discussion of the components responsible for azimuthal variations, we now focus on the smaller perturbations to the E ring's vertical structure. These perturbations arise from weak normal forces which influence only the elements i, Ω, and ω. We start by discussing Figs. 3 and 4, simulations that do not include the effects of the aligned quadrupole, for simplicity (*i.e.*, $g_{2,0}$ is artificially set to zero), although our derivations are general and will allow us to return to the important influence of the quadrupole term shortly. Perhaps the most unusual behavior displayed by the elements i, Ω, and ω in Figs. 3 and 4 is the fact that argument of pericenter locks alternately to $\omega = +90°$ when pericenter is above the equatorial plane (Fig. 1b) and to $\omega = -90°$ when pericenter is below the plane. This locking is correlated with the solar position so that the orbital pericenter is always displayed to the same side of the equatorial plane as the Sun. In all figures the Sun starts at its maximum elevation above the equatorial plane (the summer solstice in Saturn's northern hemisphere) and remains above the plane for one quarter of its orbital period of ~29.5 years, crossing the equatorial plane at $t \approx 7.4$, 22.1, and 36.9 years.

At first sight this locking may seem unimportant: since inclinations are small, what difference does it make that pericenter is always elevated out of the equatorial plane by a few tenths of a degree? There are several answers to this question. First, since these orbits periodically become highly eccentric, an E ring particle can dip in very close to the main Saturnian ring system. Because the main rings are so thin (Cuzzi *et al.* 1979), however, even small inclinations cause E ring grains to rise well above the main rings and hence collisions with these rings can only take place at orbital nodes. Locking the pericenter to ±90° puts both the nodes along the latus rectum of the ellipse (Fig. 1), maximizing the ability of an orbit of a given eccentricity to avoid intersecting the inner rings. Additionally, pericenter locking alters the probability for an impact into a Saturnian satellite since most lie at low inclinations relative to Saturn's equator. Most notably, this phenomenon enhances the probability of reimpact into Enceladus since an E ring particle's node lies at a radial distance $a(1 - e^2)$ which, for small e, is very close to Enceladus' orbit at $r =$

a. Finally, and perhaps most interestingly, this dynamical effect suggests that the vertical structure of the E ring is time-variable over a single orbit of Saturn around the Sun. Before discussing the ramifications of this time variability, we wish to understand the locking analytically.

The behavior of ω suggests that the angle is attracted to a stable equilibrium point, and so we seek such a solution. First, however, we note that there are several places in Fig. 4 (*e.g.*, near t = 7, 13, 22, . . . years) where the argument of pericenter is not strongly locked to its equilibrium value; in these locales, oscillations in ω are large and circulation can occur. These deviations happen either when the Sun passes through the equatorial plane (roughly every 15 years) and argument of pericenter begins its transfer from one equilibrium value to the next or when the orbital eccentricity is small, in which case pericenter is poorly defined and can circulate rapidly as predicted by the final term in Eq. (31). To avoid these problems, we choose initially to study the locking effect for nonzero and constant values of e and s_z, ignoring the time-dependence of these parameters. We return to justify and relax this approximation shortly. Setting $\omega_{eq} = \pm 90°$ (the subscript "eq" stands for equilibrium) and remembering that inclination must be positive, we find that Eq. (27e) is zero only when

$$\sin i_{eq} = \left| \frac{Z}{\dot{\omega}_{xy}} \right| \tag{33a}$$

which, from Eq. (27d), leads to

$$\left. \frac{d\Omega}{dt} \right|_{eq} = \dot{\Omega}_{xy} + \dot{\omega}_{xy}. \tag{33b}$$

Finally, setting Eq. (27e) equal to zero and utilizing Eq. (33a) yields an improved determination of ω_{eq}:

$$\sin \omega_{eq} = \text{sign}(\dot{\omega}_{xy}/Z). \tag{33c}$$

We check the solution given by Eqs. (27c–e) for stability by linearizing it about the equilibrium point. Here we set $\Psi = \Psi_{eq} + \Delta\Psi$, where Ψ is any of i, Ω, and ω, to find

$$\left\langle \frac{d\,\Delta i}{dt} \right\rangle = -i_{eq}\dot{\omega}_{xy}\,\Delta\omega, \tag{34a}$$

$$\left\langle \frac{d\,\Delta\Omega}{dt} \right\rangle = -\frac{\dot{\omega}_{xy}\,\Delta i}{i_{eq}}, \tag{34b}$$

$$\left\langle \frac{d\,\Delta\omega}{dt} \right\rangle = \frac{\dot{\omega}_{xy}\,\Delta i}{i_{eq}}, \tag{34c}$$

which can be trivially solved to yield

$$\Delta i = i_{eq}\omega_0 \cos(\dot{\omega}_{xy}t + \zeta_0), \tag{35a}$$

$$\Delta\Omega = -\omega_0 \sin(\dot{\omega}_{xy}t + \zeta_0), \tag{35b}$$

$$\Delta\omega = \omega_0 \sin(\dot{\omega}_{xy}t + \zeta_0), \tag{35c}$$

where the initial conditions ω_0 and ζ_0 are independent of i, Ω, and ω. Thus oscillations about the equilibrium point are stable and have frequency $\dot{\omega}_{xy}$ which, for the parameters of Fig. 4, corresponds to a period of ~1 year. The fact that the oscillation period is short compared to the characteristic periods of e and s_z justifies our earlier treatment of these latter parameters as constants; since e and s_z both change slowly with time, the rapid oscillations are able to stay centered on the slowly drifting equilibrium value. These results, Eqs. (33)–(35), seem to be in good agreement with Figs. 3 and 4. Equation (33c) correctly predicts that pericenter and the Sun always lie on the same side of the equatorial plane since $\dot{\omega}_{xy} > 0$ and, with no quadrupole term, Z changes sign every time the Sun crosses the equatorial plane. Furthermore, Eq. (33a) shows that the inclination approaches zero when Z is small which occurs either when the Sun is in the ring plane or when $e \to 0$, as we already inferred from Figs. 3 and 4. Additionally, several features of Eqs. (35a–c) can be checked against the full numerical integrations. As expected, the oscillations in all three elements have eccentricity-dependent periods of approximately 1 year and, as predicted by Eq. (31), this period decreases for large eccentricities (the inclination trace in Fig. 4 provides a nice example). Furthermore, since no discernible oscillations appear in the solar angle, which is basically the sum of Ω and ω, the oscillations in these angles must be equal in magnitude and 180° out of phase as predicted by Eqs. (35b,c). Additionally, we find that the i oscillations peak one-quarter of a period before the ω oscillations as predicted by Eqs. (35a,c), although the phase difference is difficult to detect in these figures.

We now add the effects of the aligned quadrupole term to the array of forces influencing the dust grain. Figure 5 shows the orbital history of a grain with the same properties and initial conditions as the particle in Fig. 4; the only change is that the magnetic field from which the Lorentz force is calculated now includes the aligned quadrupole component. The eccentricity and solar angle traces in Fig. 5 are basically unchanged from Fig. 4, but the i, Ω, and ω traces are substantially altered. Inclinations of nearly a degree (three times larger than in Fig. 4) are attained—the effects of the quadrupole term are definitely important for Saturn's E ring! Furthermore, the pericenter favors locking to −90° over locking to 90°; this can be easily explained by considering how the addition of the quadrupolar term changes Z. Using the values given in the figure captions, we find that the second term in Eq. (32) is always negative and, for small e, its magnitude

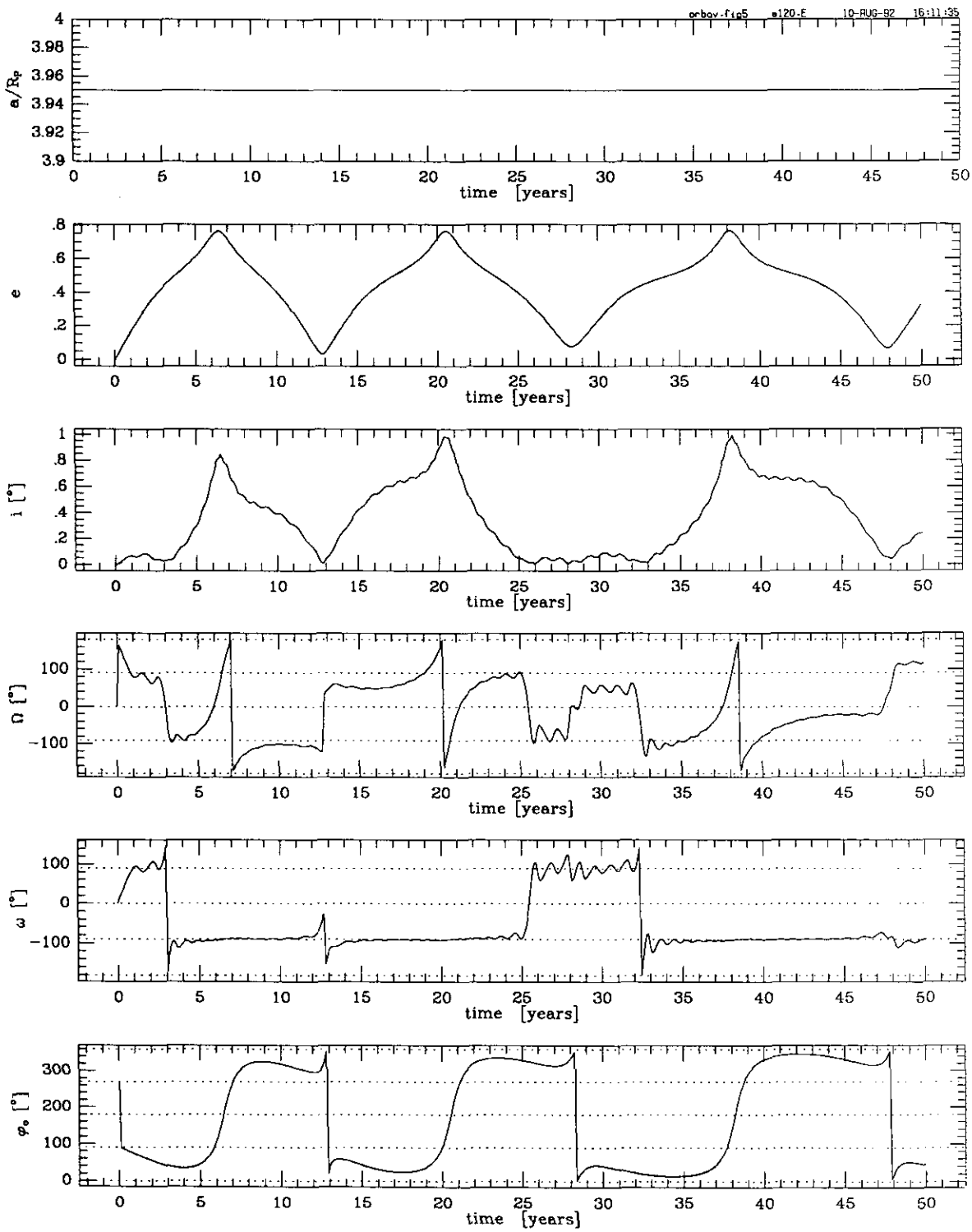

FIG. 5. Osculating orbital elements plotted against time from integrations of the orbit-averaged equations of motion. Again, the results agree well with the full Newtonian integrations, which are not shown. Initial conditions and numerical quantities are the same as in Fig. 4, but the additional effects of the aligned magnetic quadrupole have been included. Note the striking difference in the i and ω traces in the two figures. The magnetic field coefficients used for Saturn are $g_{1,0} = 0.2154$ G and $g_{2,0} = 0.0164$ G (*cf.* Connerney *et al.* 1984).

is less than the maximum value of the first. Thus Z is predominantly negative and, as predicted by Eq. (33c), ω is usually found near $-90°$. When the Sun is high above the equatorial plane, however, Z is positive and ω locks to 90° as observed in Fig. 5. Since the two terms in Z have different eccentricity dependencies, the time spent with $\omega \sim 90°$ will vary from one occasion to the next. This same sharp eccentricity dependence of the quadrupole contribution to Z is also responsible for the difference in maximum inclinations observed between Figs. 4 and 5.

If all E ring particles originated from Enceladus and had parameters like those chosen for Fig. 5, we would expect that inner portions of the ring (the pericenter sides of instantaneously elliptical orbits) would be offset to the south of the equatorial plane when the Sun is not too far to the north. The outer portions of the ring, of course, would be offset in the opposite direction. There is not a single solar position at which orbits transfer from one equilibrium to the next; as the Sun rises in the northern sky, orbits with low eccentricities switch first, followed by those with greater eccentricities. In addition, a more realistic ensemble of different particle sizes and shapes would cause further smear in the time when orbits switch equilibria since α and L vary significantly with particle properties. So when the Sun is to the north of the equatorial plane, the situation is difficult to assess. Conversely, when it is to the south, Z is negative and all orbits in the ensemble should have their pericenters depressed toward the south.

Adding in different initial conditions and additional satellite sources for E ring particles further complicates the issue; these factors can cause the initial conditions to be far from the equilibrium point. When this is true, the oscillations in ω can be large enough to cause circulation of that element and this washes out the asymmetry discussed above. Assuming that dust grains originate from satellites, they will always start on nearly circular orbits for which the equilibrium inclination is $i_{eq} = 0$ (Eqs. 32 and 33a). Several effects can cause initial inclinations to differ from zero, most notably the small underlying inclination of the source satellite itself, and the dispersion of grain launch velocities. We find, numerically, that initial inclinations of more than about 0.5° for grains launched from either Enceladus or Tethys cause oscillations large enough to destroy the locking. This cutoff can also be found analytically from Eq. (27e). It is reasonable to assume that most of the grains escape from their source moon with the minimum possible energy; in this case escape will occur along the Saturn-satellite line (*cf.* Hamilton and Burns 1991) with minimal change to the initial inclination. The orbits of Enceladus and Dione are negligibly inclined, but those of Tethys and Mimas have inclinations that exceed a degree; thus nominally grains launched from Enceladus will have their pericenters locked while those from Tethys will not. Summing the contributions of several source satellites and different initial conditions complicates the picture, but we believe that some vertical asymmetry and time variability are likely to remain.

7. DISCUSSION

In the preceding sections, we have explored the orbital dynamics of micrometer-sized dust grains both numerically and analytically, and argued for azimuthal and vertical asymmetries in Saturn's E ring. In this section we apply our new understanding of the dynamics of E ring dust grains to the problems of the ring's breadth and height mentioned in Section 6.1; we then conclude by discussing the possibility for further ground-based and spacecraft observations.

In contrast to the linear model of Horanyi *et al.* (1992), the nonlinearity of the orbit-averaged equations considered here causes some orbits with nearly maximum eccentricities to be oriented perpendicular to the Sun–Saturn line. Thus our model suggests that the E ring, as seen from Earth, displays nearly its full breadth. This correction may be enough for a primary source of dust grains at Enceladus and a weaker source at Tethys ($a \approx 4.89R_p$) to account for the full width of the E ring as observed from Earth. An additional source at Tethys is also consistent with the extra material seen in the vicinity of that moon (Showalter *et al.* 1991, Fig. 11). Finally, the vertical structure discussed above may provide further dynamical evidence for a secondary source of particles from Tethys. If Enceladus were the ring's only source, our numerical simulations would predict maximum thicknesses of about 7,500 km (if orbital pericenters are locked) and 15,000 km (if pericenters are not locked). These numbers are three times larger than those predicted by the Horanyi *et al.* (1992) model which neglected the quadrupole term of the magnetic field; clearly this term cannot be ignored! As noted above, however, the E ring is about 40,000 km thick at its outer edge, still quite a bit broader than our predictions based on Fig. 5. Grains launched from Tethys, however, attain inclinations of ~2.5° and, because of Tethys' relatively large orbital inclination, the orbital pericenters are not locked. When combined, these effects lead to a predicted thickness of $\gtrsim$40,000 km at the outer edge of the E ring, a figure that is in agreement with the observations.

Could other mechanisms, most notably Lorentz resonances, provide the increase in thickness without an additional Tethys source? While most of the strongest Lorentz resonances lie very close to Saturn, we note that just interior to Enceladus there is an important 3 : 1 resonance driven by the tilted dipolar field whose strength is proportional to $eig_{1,1}$ (Hamilton and Burns 1993a). Simulations, in which we assume a 0.8° tilt in Saturn's magnetic dipole,

indicate that the inclination of some Enceladus-launched grains can be pumped up to a few degrees. During this process, the locking of the orbital pericenter, which leads to the vertical asymmetry, can be broken. Thus we conclude that while a Tethys source accounts nicely for the observed inclinations, the 3 : 1 Lorentz resonance acting on material launched from Enceladus may also be able to do so. In either case, however, the breath of the E ring still argues for a Tethys source.

Can the azimuthal and vertical asymmetries discussed in Sections 6.2 and 6.3 be observed from the ground or from spacecraft? The most favorable time for ground-based observations of the E ring occurs when Saturn's main rings, as seen from Earth, appear edge-on; this last occurred in 1979–1980 and will next happen in 1995–1996. Because the predicted azimuthal asymmetry of the E ring is most clearly present when the dimensions in the solar and antisolar directions are compared and is less visible in the perpendicular directions, it is very unlikely that azimuthal asymmetry can be seen from the ground during these times. Although the vertical asymmetry should, technically, be visible from Earth, the magnitude of the effect may be too small to be noticeable. When the Sun is nearly in the ring plane, the quadrupole dominates pericenter locking and dust exterior to Enceladus' orbit ($a = 3.95R_p$) should be offset slightly to the north; interior to Enceladus it should be found slightly to the south. The magnitude of the offset depends on the unknown properties of the ensemble of grains that make up the E ring; offsets should increase, however, with radial distance from Enceladus.

There are definite hints of vertical asymmetry from the Voyager flyby missions. Showalter *et al.* (1991) cite evidence from Voyager images centered at about $4R_p$ for a northern offset of several hundred kilometers—larger than that expected by the differences between the equatorial and Laplace planes. The offset predicted by Eqs. (33a–c) is small at this distance because it is just outside the position where the orbital nodes lie. Since the Sun was elevated only ~4° north of the equatorial plane at the time of the flyby, the quadrupole term should still dominate the solar term and material exterior to the nodes should be elevated slightly to the north as observed. In addition, Voyager 1 swept through the E ring at a distance of about $6.1R_p$, near the Dione "clear zone," and returned data from its PWS instrument, which was discovered to be sensitive to dust impacts. These data imply an offset to the south (W. Kurth, private communication, 1992). Most of the material in this region probably originates from Tethys, in which case the orbital pericenters are not locked; thus we cannot easily predict the sense of the observed offset.

Questions about the sources of dust and possible asymmetries in the E ring's structure are difficult to answer from ground-based observations alone. Because single particle dynamics dominates collective effects in the E ring, detailed information on individual particle orbits, which can most easily be obtained from spacecraft observations, is desirable. The sources of E ring material should be easily identified when the Cassini orbiter, with its sophisticated dust detector, arrives at Saturn and makes repeated passes through the region. The mission should also be able to determine the nature and extent of any azimuthal and vertical asymmetry.

8. ACKNOWLEDGMENTS

I am deeply indebted to Joseph A. Burns for many insightful discussions and for several critical readings of this text. Thanks are also due to Leslie E. Schaffer for constructive criticism and to two anonymous referees whose comments were especially helpful. I would also like to acknowledge a useful conversation with Mihaly Horanyi. This work was supported by NASA Grant NAGW-310.

REFERENCES

ACUÑA, M. H., K. W. BEHANNON, AND J. E. P. CONNERNEY 1983. Jupiter's magnetic field and magnetosphere. In *Physics of the Jovian Magnetosphere* (A. J. Dessler, Ed.), pp. 1–50. Cambridge Univ. Press, New York.

BAUM, W. A., T. KREIDL, J. A. WESTPHAL, G. E. DANIELSON, P. K. SEIDELMANN, D. PASCU, AND D. G. CURRIE 1981. Saturn's E ring. I. CCD observations of March 1980. *Icarus* **47,** 84–96.

BORDERIES, N., AND P.-Y. LONGARETTI 1987. Description and behavior of streamlines in planetary rings. *Icarus* **72,** 593–603.

BURNS, J. A., AND L. E. SCHAFFER 1989. Orbital evolution of circumplanetary dust by resonant charge variations. *Nature* **337,** 340–343.

BURNS, J. A., P. L. LAMY, AND S. SOTER 1979. Radiation forces on small particles in the solar system. *Icarus* **40,** 1–48.

BURNS, J. A., L. E. SCHAFFER, R. J. GREENBERG, AND M. R. SHOWALTER 1985. Lorentz resonances and the structure of the Jovian ring. *Nature* **316,** 115–119.

CHAMBERLAIN, J. W. 1979. Depletion of satellite atoms in a collisionless exosphere by radiation pressure. *Icarus* **39,** 286–294.

CONNERNEY, J. E. P., L. DAVIS, JR., AND D. L. CHENETTE 1984. Magnetic field models. In *Saturn* (T. Gehrels and M. S. Matthews, Eds.), pp. 354–377. Univ. of Arizona Press, Tuscon.

CUZZI, J. N., J. A. BURNS, R. H. DURISEN, AND P. HAMILL 1979. The vertical structure and thickness of Saturn's rings. *Nature* **281,** 202–204.

DANBY, J. M. A. 1988. *Fundamentals of Celestial Mechanics* (2nd ed.). Willmann–Bell, Richmond, VA.

GOERTZ,, C. K., 1989. Dusty plasmas in the solar system. *Rev. Geophys.* **27,** 271–292.

GREENBERG, R. 1981. Apsidal precession of orbits about an oblate planet. *Astron. J.* **86,** 912–914.

GURNETT, D. A., E. GRÜN, D. GALLAGHER, W. S. KURTH, AND F. L. SCARF 1983. Micron-sized particles detected near Saturn by the Voyager plasma wave instrument. *Icarus* **53,** 236–254.

GURNETT, D. A., W. S. KURTH, F. L. SCARF, J. A. BURNS, J. N. CUZZI, AND E. GRÜN 1987. Micron-sized particle impacts detected near Uranus by the Voyager 2 plasma wave instrument. *J. Geophys. Res.* **92,** 14,959–14,968.

GURNETT, D. A., W. S. KURTH, L. J. GRANROTH, AND S. C. ALLENDORF 1991. Micron-sized particles detected near Neptune by the Voyager 2 plasma wave instrument. *J. Geophys. Res.* **96,** 19,177–19,186.

HAMILTON, D. P., AND J. A. BURNS 1991. Orbital stability zones about asteroids. *Icarus* **92,** 118–131.

HAMILTON, D. P., AND J. A. BURNS 1992. Orbital stability zones about asteroids. II. The destabilizing effects of eccentric orbits and of solar radiation. *Icarus* **96,** 43–64.

HAMILTON, D. P., AND J. A. BURNS 1993a. Lorentz resonances. In preparation.

HAMILTON, D. P., AND J. A. BURNS 1993b. A steady state collisional model for Saturn's E ring. In preparation.

HORANYI, M., AND J. A. BURNS 1991. Charged dust dynamics: Orbital resonance due to planetary shadows. *J. Geophys. Res.* **96,** 19,283–19,289.

HORANYI, M., J. A. BURNS, AND D. P. HAMILTON 1992. The dynamics of Saturn's E ring particles. *Icarus* **97,** 248–259.

KOZAI, Y. 1959. The motion of a close Earth satellite. *Astron. J.* **64,** 367–377.

LARSON, S. M., J. W. FOUNTAIN, B. A. SMITH, AND H. J. REITSEMA 1981. Observations of the Saturn E ring and a new satellite. *Icarus* **47,** 288–290.

MEYER-VERNET, N. 1982. "Flip-flop" of electric potential of dust grains in space. *Astron. Astrophys.* **105,** 98–106.

MIGNARD, F. 1982. Radiation pressure and dust particle dynamics. *Icarus* **49,** 347–366.

MIGNARD, F. 1984. Effects of radiation forces on dust particles in planetary rings. In *Planetary Rings* (R. Greenberg and A. Brahic, Eds.), pp. 333–366, Univ. of Arizona Press, Tucson, AZ.

SCHAFFER, L. E., AND J. A. BURNS 1987. The dynamics of weakly charged dust: Motion through Jupiter's gravitational and magnetic fields. *J. Geophys. Res.* **92,** 2264–2280.

SCHAFFER, L. E., AND J. A. BURNS 1992. Lorentz resonances and the vertical structure of dusty rings: Analytical and numerical results. *Icarus* **96,** 65–84.

SCHAFFER, L. E., AND J. A. BURNS 1993. Stochastic charging and its effect on Lorentz resonances in planetary rings. *J. Geophys. Res.*, in press.

SHOWALTER, M. R., J. N. CUZZI, AND S. M. LARSON 1991. Structure and particle properties of Saturn's E ring. *Icarus* **94,** 451–473.

SMYTH, W. H., AND M. L. MARCONI 1993. The nature of the hydrogen tori of Titan and Triton. *Icarus*, **101,** 18–32.